Carbon Capture Science & Technology 8 (2023) 100118

Contents lists available at ScienceDirect

Carbon Capture Science & Technology

journal homepage: www.elsevier.com/locate/ccst

Full Length Article

Modelling of photocatalytic CO_2 reduction into value-added products in a packed bed photoreactor using the ray tracing method

Amirmohammad Rastgaran[a], Hooman Fatoorehchi[a], Navid Khallaghi[b], Afsanehsadat Larimi[c], Tohid N. Borhani[d,*]

[a] Department of Chemical Engineering, Tehran University of Technology, Tehran, Iran
[b] Department of Chemical Engineering, The University of Manchester, UK
[c] Department of Chemical and Process Engineering, Niroo Research Institute, Tehran, Iran
[d] School of Engineering, Center for Engineering Innovation and Research, School of Engineering, Computing and Mathematical Sciences, University of Wolverhampton, UK

ARTICLE INFO

Keywords:
CO_2 photoreduction
Computational fluid dynamics
Mathematical modelling
Simulation
Optics
Packed bed reactor

ABSTRACT

This research suggests a comprehensive 3D model for modelling photocatalytic conversion of CO_2 to methane, hydrogen and carbon monoxide in a packed bed reactor. This research includes two parts: designing the reactor's geometry using a new method in "blender" and using the computational fluid dynamics (CFD) technique to study and analyse the reaction, transport of phenomenon and light intensity through the reactor. Laminar flow, chemical reaction, mass transfer and optics physics were considered together to solve the equations. The surface reaction in the reactor follows a modified version of the Langmuir-Hinshelwood equation that evaluates the light profile in the reactor and the blockage of the catalyst's surface over time. Thus, a new method for 3D modelling light profiles in the reactor is introduced. The rate of reaction continues to increase with the pressure, and after 1 atm, the rate becomes steady. In the first 17 h, the methane rate is the highest, and then the carbon monoxide rate overcomes the methane rate. The rate of hydrogen is considerably lower than the other products. Changing pellets from spheres to Raschig rings causes growth in the probability density function (PDF) at the first moments. In methane's PDF, the amount of Raschig and sphere are 0.25 and 0.18, respectively, at the start of the reaction. Thus, the Raschig ring operates more effectively at the beginning moments of the process but eventually is outweighed after an hour by spherical particles. In the end, the validation of modelling and results were investigated with the aid of experimental data.

1. Introduction

Reducing the harmful effects of CO_2 on the environment is a global challenge that needs to be addressed with precise methods and solutions. Some of the potential risks engaged with increasing CO_2 emissions are highlighted by The Synthesis Report of the Intergovernmental Panel on Climate Change (IPCC) (IPCC, 2014). Using modern farming methods, renewable energy and improving energy efficiency in industrial plants and buildings can impact CO_2 emissions significantly (Roberts et al., 2018). Direct air capture has become a feasible way to decrease CO_2 emissions in the atmosphere (Fasihi et al., 2019). Another practical approach to reducing CO_2 is capturing it at the source point using different methods such as absorption, adsorption, membrane, calcium looping, etc. (Vitillo et al., 2017; Borhani and Wang, 2019). Both mentioned capturing approaches require underground/undersea storage.

Conversion of CO_2 to value-added products with solar light is an effective way to cope with environmental crises and complete the carbon cycle (Nematollahi et al., 2019; Nematollahi et al., 2020; Moradi et al., 2019; Moradi et al., 2020; Larimi and Khorasheh, 2020). There are different methods to convert CO_2 to fuels and value-added products, such as dry reforming of methane, reverse water-gas shift reaction, CO_2 methanation and electrochemical CO_2 reduction (Yao et al., 2020; Garba et al., 2021; Whang et al., 2019; Pakhare and Spivey, 2014; Chen et al., 2017; Zhu et al., 2016). The conversion of CO_2 to hydrocarbon fuels by the photocatalytic process has gained lots of research interest in recent years (Creutzig et al., 2017; Alsayegh et al., 2020).A number of researches have been carried out on photo-reduction of CO_2 using H_2O on powdered TiO_2 at room temperature to form CO_2 and CO simultaneously (Olivo et al., 2015; Zhang et al., 2021). CO_2 is a very stable molecule due to its high bond energy (750 kJ mol^{-1}), requiring high temperatures for thermo-catalytic conversion. However, a different possible approach is to convert CO_2 by aid of light (photocatalysis). The redox potential for a single electron transfer to CO_2 is considerably high (−1.85 eV) due to the fact that bending a linear CO_2 molecule and inject-

* Corresponding authors.
E-mail addresses: Hfatoorehchi@ut.ac.ir (H. Fatoorehchi), t.borhani@wlv.ac.uk (T.N. Borhani).

https://doi.org/10.1016/j.ccst.2023.100118
Received 19 April 2023; Received in revised form 26 May 2023; Accepted 30 May 2023

Nomenclature

Symbol	*Definition unit*
p_i	partial pressure kpa
K_i	equilibrium adsorption constants 1
k	rate constant 1
a_i	the number of moles for each reactant from the assumed surface reaction 1
ρ	density g/m^3
u	velocity m/s
p	pressure kpa
F	force N
I	light intensity W/m^2
η	deactivation scale parameter 1
α	reaction order of light intensity 1
t	time h
J	diffusive molar mass flux mole/(h.m^2)
c	concentration mole/m^3
R	surface reaction rate μmole/(h.m^2)
D	diffusion coefficient m^2/s
C	correction coefficient 1
S	surface area m^2
$R_{st.st}$	imaginary steady state part of reaction μmole/(h.m^2)

ing an electron into its orbitals is unfavourable. Most semi-conductors have higher conduction band (CB) than the redox potential. Although on some catalysts CO_2 can transform in a bent configuration. Despite the relatively high temperature and pressure (at least 500 K and 10 bar) in the thermo-catalytic process, photocatalysis can take place at room temperature and atmospheric pressure (Kovačič et al., 2020; Gandhi et al., 2022). Photoreduction of CO_2 represents a way to force CO_2 to bend its linear shape and create dipole moments, potentially leading to chemical reactivity; however, due to its low conversion, the major focus is on developing efficient photocatalysts for CO_2 photoreduction (Ji and Luo, 2016; Li et al., 2016; Ola and Maroto-Valer, 2015).

Typically, two photoreactors are used for the photocatalytic conversion of CO_2 into fuel: slurry and immobilised reactors (Asadi et al., 2022). In a slurry-bed reactor, catalysts are homogeneously dispersed in the target solution, and mechanical stirring could potentially enhance photocatalytic efficiency. However, one drawback of this type of reactor is the loss of catalysts during the recycling process. Consequently, performing a sequential modification test on the same photocatalyst for comparison is difficult.

Immobilised packed bed reactors (PBRs) are simple to construct and do not require recycling. Despite the slurry reactor, the scattering and absorption effect of the solution do not reduce light intensity through the reactor, and a light transparent substrate is used to deliver light directly to the photocatalyst. Ease of operation and better product quality control are other advantages of PBRs (Ji and Luo, 2016; Li et al., 2016). However, modelling the photoreduction of CO_2 in a packed bed reactor suffers from several issues that must be addressed. First, the interaction between fluid and packed bed particles makes a complex flow regime in the system, challenging the estimation of fluid behaviour (Baker, 2011). Also, many factors are involved in the reaction rate, and the currently available data for this exact reaction significantly depends on operation parameters. Yet, the lack of a comprehensive kinetic model makes this procedure difficult, and there are limited examples of photo-reduction kinetic studies (Ali et al., 2019; Thompson et al., 2020a; Delavari and Amin, 2016; Khalilzadeh and Shariati, 2018; Kwon et al., 2016; Shakeri et al., 2015; Shown et al., 2018; Tahir and Amin, 2015; Tan et al., 2017). Also, the reaction is engaged with undesired products blocking the surface, which leads to considerable changes in the reaction rate over time. The other issue is that the light intensity through the reactor has a substantial impact on the reaction rate, so optics modelling is inevitable. Therefore, finding a precise method to calculate light intensity is the main focus of this research.

Based on the conditions, there are different methods to calculate light intensity. The Lambert-Beer law is one of the leading theories on which much optics modelling literature is based (Aal E Ali et al., 2022; Martin et al., 2020; Mazarji et al., 2017; Szyman, 2021). According to the Lamber-Beer Law, transmittance depends on the molar concentration of the solution, path length and light intensity. The Lamber-Beer Law is also one of the fundamental theories of optical spectrometers (Mamouei et al., 2021). Analytical approach to predict the light profile inside a reactor could only be used in geometrically simple reactors such as a monolith reactor, where a catalytically active thin film is coated on the inner walls of monolith channels (Hossain and Raupp, 1998). None of the previous methods works for a randomly packed bed reactor since the Lamber-Beer law is only valid for solutions, and developing an analytical solution is impossible due to randomly placed particles. Therefore, the Ray tracing technique has been proposed to calculate the intensity profile and couple it with CFD.

Nowadays, ray tracing is widely used in artistic designs, movies and video games to simulate real word situations of light distribution. Also, there is research in solar systems, such as modelling direct solar radiation in the compound parabolic collector to see how the rays behave (Mazarji et al., 2017). In this research, a novel method has been proposed to calculate intensity using the ray tracing technique. The results of the rays' trajectory and intensity through the reactor are apparent; however, the computational cost of this method is approximately high. The reactor has numerous transparent particles, so each ray may pass through several particles. When a ray hits a particle, some of its energy reflects, and the rest passes through the particle, increasing the ray's number exponentially. Furthermore, due to the randomness of the reactor's particles, 3-D modelling is vital, and the number of rays must be sufficient to achieve a natural light profile on the pellet's surface. As a result, the amount of calculation is tremendously high, which thanks to recent development in processor's units has become feasible. This method has the potential to become a useful tool for any types of photocatalytic reactor design.

Although several practical investigations have been performed so far, there are only a limited number of research on the theory of PBRs for the CO_2 reduction reaction. Hence, this research aims to fill this knowledge and data gaps and address the above-mentioned issues. Computational fluid dynamics (CFD) is employed to model the packed bed reactors as it provides a better insight into the flow patterns in the reactor (Asadi et al., 2022; Jiang et al., 2002). First, a laminar model was used for the fluid flow, and the case was modelled in the low Reynolds number to avoid further complexity in the flow regime. Also, since the time-dependant modelling for this case is simply impossible, a semi-time-dependant approach has been used by dividing the model into the imaginary steady state (transport of phenomenon) and time-dependant (optic) part. Furthermore, a novel method based on ray tracing has been introduced for 3D optics modelling, simulating real-world situations by tracing a significant number of rays through the reactor.

2. Model equations

Laminar flow, chemical reaction, mass transfer and optics equations are required to solve together to acquire a comprehensive model of photo-conversion of CO_2 in a packed bed reactor. This model includes velocity, pressure and concentration through the reactor and surface reaction rates on the particles' surface and their changes over time.

2.1. Laminar flow equation

The flow is assumed to be vertical, incompressible, steady, and isothermal. Due to the low Reynolds number, the laminar flow equation is used in this modelling. Navier–Stokes and continuity equations are

applied for the mathematical description of the viscous fluid through a three-dimensional packed bed reactor. By considering gravity force and constant viscosity, the microscopic equations of motion can be written in the following form:

$$\rho\nabla\cdot\mathbf{u}=0 \tag{1}$$

$$\rho u\cdot\nabla u=-\nabla p+\mu\nabla\cdot\nabla u+\rho g \tag{2}$$

where p, u, ρ, g and μ represent the fluid's pressure, velocity, density, gravity and dynamic viscosity, respectively. The flow has a uniform velocity profile (U_O = 2 cm/s) at the inlet, and the outlet's pressure is assumed to be fixed to the local atmospheric pressure (p = 1.1atm). Furthermore, the no-slip boundary condition is considered for the entire solid-fluid interface.

2.2. Reactions

A modified model of Langmuir–Hinshelwood was used in this study to account for chemical reactions. Aside from the partial pressure of CO_2 and H_2O, the deactivation of the catalyst's sites over time is taken into account in this model (Thompson et al., 2020b). There is evidence that the main reason for catalyst deactivation is the formation of bidentate carbonate species, peroxo and peroxocarbonate species on the photocatalyst's surface. One way to explain a catalyst's deactivation over time is to assume elementary surface reactions permanently deactivate active sites and then integrate these reactions over time to estimate the concentration of sites that deactivate over time. However, acquiring a comprehensive deactivation model is not yet possible due to the lack of knowledge about the causes of deactivation, so a macroscopic-based kinetic model is used here without consensus on the driving force behind the deactivation (Fresno et al., 2018).

$$r=k\cdot PDF(t)\frac{\prod_{i=1}^{n}\left(K_iP_i\right)^{a_i}}{\left(1+\sum_{i=1}^{z}K_iP_i\right)^{\Sigma a_i}} \tag{3}$$

This equation includes steady-state and time-dependant terms, PDF(t). The first term is a function of partial pressures, which is the general format of Langmuir–Hinshelwood, and the second term is a function of time which considers the deactivation of the catalyst's sites over time. The overall rate of surface reaction is defined for the surface unit ($\mu mol.cm^{-2}.h^{-1}$).

2.2.1. Unsteady state part of reaction rate PDF(t)

The chance of photons reaching active sites is the key element for assessing all the phenomena involved in the photocatalytic process. Probability density function (PDF) represents how likely it is that the photons reach the active sites which is decreasing over time by forming undesired by-products blocking the active sites. PDF(t) is driven by a statistical function named the Weibull function. It depends on two parameters (η and β). β is the shape parameter and η is the scale parameter and both of them have a direct relationship with height and broadness of the Weibull PDF(t) consequently:

$$PDF(t)=\frac{\beta}{\eta}\left(\frac{t}{\eta}\right)^{\beta-1}\exp^{-\left(\frac{t}{\eta}\right)^{\beta}} \tag{4}$$

$$\beta=I^{\alpha} \tag{5}$$

$$PDF(t)=\frac{I^{\alpha}}{\eta_d}\left(\frac{t}{\eta_d}\right)^{I^{\alpha}-1}\exp^{-\left(\frac{t}{\eta_d}\right)^{I^{\alpha}}} \tag{6}$$

Weibull function is re-parametrized to include illuminated active sites and a deactivation term. η represents the impact of deactivation (η_d) which has direct relationship with photons reaching active sites where β is analogous to the impact of irradiance of illuminated sites successfully catalysing the reaction (Thompson et al., 2020b).

Table 1
Reaction and the rate of products (Thompson et al., 2020b).

Product	Assumed surface reaction	LH model
CH_4	$CO_2+2H_2O\rightarrow 2O_2+CH_4$	$r_{CH_4}=k\cdot PDF(t)\frac{(K_{H_2O}P_{H_2O})^4K_{CO_2}P_{CO_2}}{(1+K_{H_2O}P_{H_2O}+K_{CO_2}P_{CO_2})^5}$
CO	$CO_2\rightarrow CO+\frac{1}{2}O_2$	$r_{CO}=k\cdot PDF(t)\frac{K_{H_2O}P_{H_2O}K_{CO_2}P_{CO_2}}{(1+K_{H_2O}P_{H_2O}+K_{CO_2}P_{CO_2})^2}$
H_2	$2H_2O\rightarrow 2H_2+O_2$	$r_{H_2}=k\cdot PDF(t)\frac{(K_{H_2O}P_{H_2O})^2}{(1+K_{H_2O}P_{H_2O}+K_{CO_2}P_{CO_2})^2}$

Table 2
Probability LH-based kinetic model coefficients (Thompson et al., 2020b).

Product	k	η_d	α	K_{H_2O}	K_{CO_2}
CH_4	7.16 × 10−1	4.81	7.37 × 10−2	99.99	3.21
CO	4.62 × 10−1	19.80	3.51 × 10−2	79.33	22.65
H_2	3.43 × 10−2	2.78	1.06 × 10−1	77.22	12.54

Table 3
Optics experimental setup data (Lo et al., 2007).

Particle's material	Corning 7740 Pyrex.
wavelength	365nm
Initial intensity	74.43 W/m^2
Number of rays	200,000
Refractive index	1.474

Table 4
Rigid body physics.

Mesh	particles	Reactor's body
Type	active	passive
Shape	Convex hull	mesh
Bounciness	0.5	0
Friction	0.1	0.1

2.2.2. Steady-state part of the reaction rate

It follows the general format of Langmuir–Hinshelwood:

$$r=k\frac{\prod_{i=1}^{n}\left(K_iP_i\right)^{a_i}}{\left(1+\sum_{i=1}^{z}K_iP_i\right)^{\Sigma a_i}} \tag{7}$$

where K_i represents the equilibrium adsorption constants for reactants and products (kpa^{-1}), and P_i refer to the partial pressures for reactants and products (kpa).

2.2.3. The overall rate of reaction

It is a combination of the two previous parts:

$$r=k\frac{I^{\alpha}}{\eta_d}\left(\frac{t}{\eta_d}\right)^{I^{\alpha}-1}\exp^{-\left(\frac{t}{\eta_d}\right)^{I^{\alpha}}}\frac{\prod_{i=1}^{n}\left(K_iP_i\right)^{a_i}}{\left(1+\sum_{i=1}^{z}K_iP_i\right)^{\Sigma a_i}} \tag{8}$$

where r is the rate of reaction ($mol.m^{-2}.h^{-1}$); k is the rate constant ($mol.cm^{-2}.h^{-1}$); I is the irradiance(dimensionless); t is time (h); η *is the* deactivation scale parameters(Dimensionless); η is the deactivation scale parameter (Dimensionless); α is the reaction order of light intensity (Dimensionless); K_i represent the equilibrium adsorption constants for reactants and products (kpa^{-1}); P_i refer to the partial pressures for reactants and products (kpa); n indicates the number of reactants involved in the assumed surface reaction; a_i is the number of moles for each reactant from the assumed surface reaction and z indicates the number of all reactants and products. Langmuir–Hinshelwood models and the amounts of parameters are shown in Tables (1) and (2).

Table 5
CFD computational models studied before.

Photoreactor	Products	CFD method	Dimension	Refs.
Fluidized bed	CO_2, H_2, CO	MP-PIC and RTE	2D axisymmetric	(Lu et al., 2022)
Twin reactor	CH_3CHO, CH_3COOH	RTE	2D axisymmetric	(Lu et al., 2021)
Bubble slurry	CH_3OH	-	2D axisymmetric	(Asadi et al., 2022)
Packed bed reactor	CO_2, H_2, CO	ray tracing N.S (laminar flow)	3D	Current study

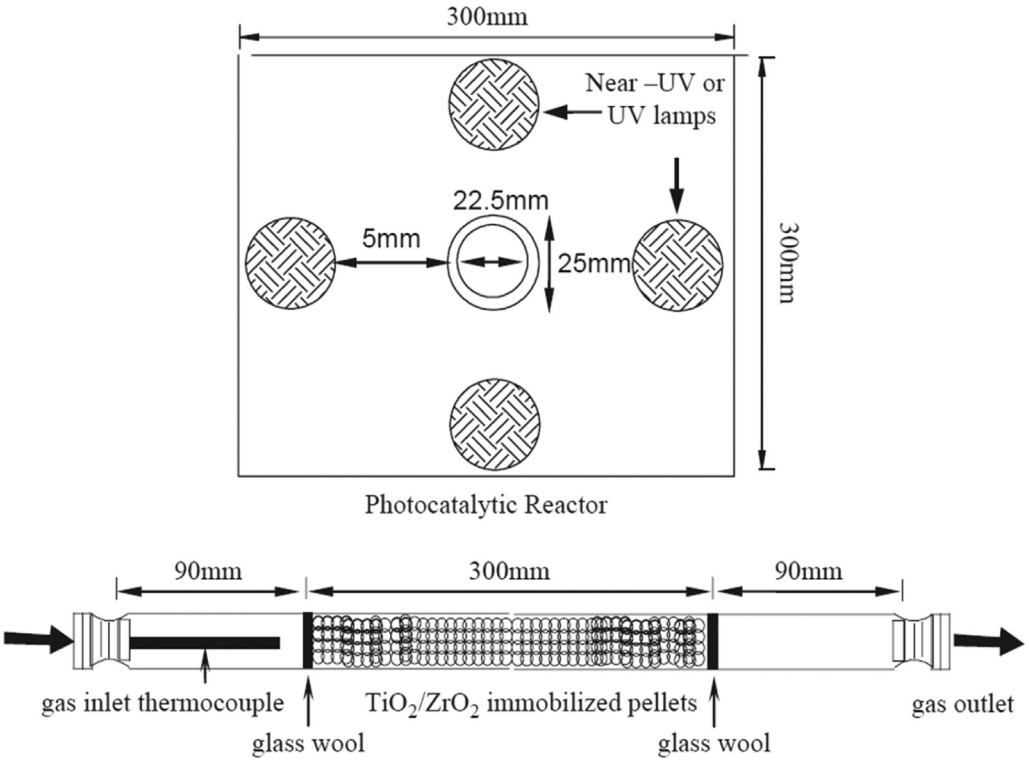

Fig. 1. Schematic of the photocatalytic reactor (Lo et al., 2007).

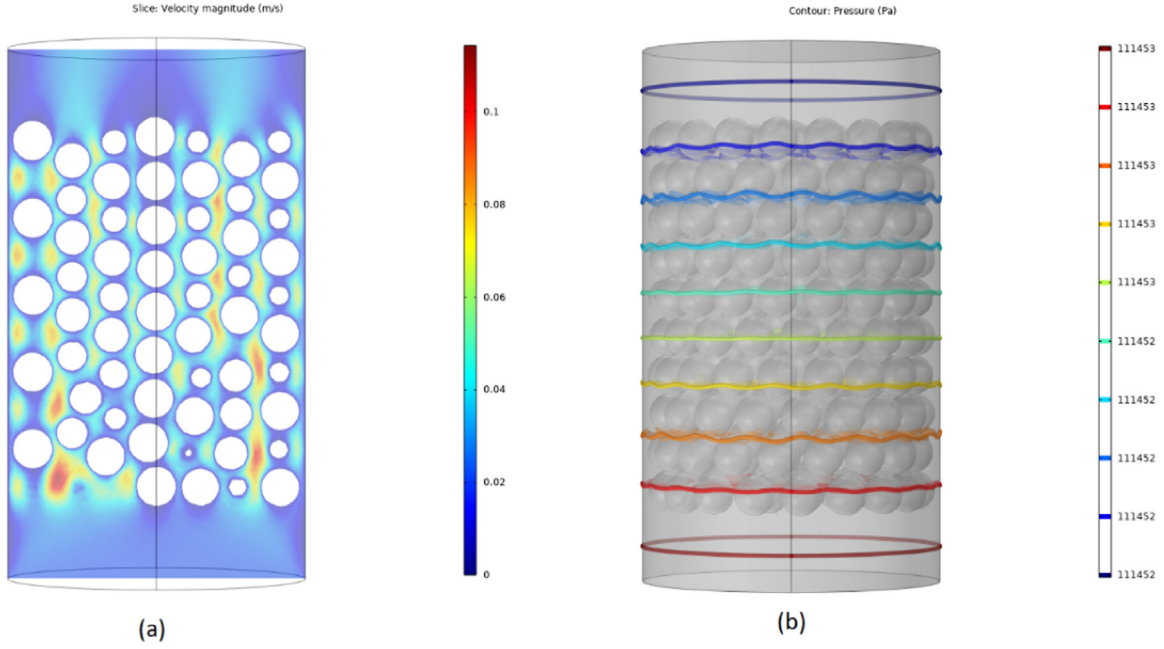

Fig. 2. (a) Velocity (m/s) and (b) pressure (Pa) profiles.

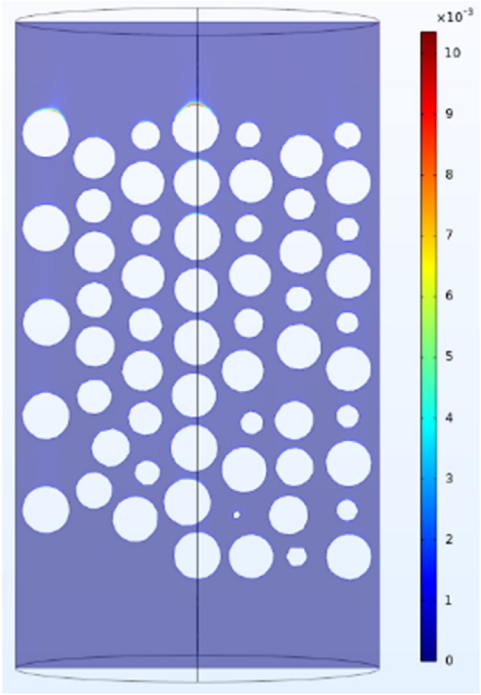

Fig. 3. Concentration (mol/m^3) of methane.

2.3. Yield

The yield of the reaction illustrates the total amount of products (μmol) per catalyst's load (gr) which follows the below equation:

$$Yield = \frac{1}{g_{cat}} \int_t \iint_s r_{st.st} PDF(s.t) ds dt. \tag{9}$$

where $r_{st.st}$ is the imaginary steady state part of reaction; s represents the catalyst's surface; t is time, and g_{cat} is the catalyst's load. Since the imaginary steady state part of the reaction is almost constant on the particles (it is shown in the result section), the equation can be rewritten like this:

$$Yield = \frac{r_{st.st}}{g_{cat}} \int_t \iint_s PDF(s.t) ds \cdot dt \tag{10}$$

The reactor is symmetrical, and there are no interactions between rays, so we can use the scale-up technique and assume the light distribution in a Longitudinal part of the reactor could represent the light distribution in the reactor. For this case, the average PDF of 1 cm of the reactor (102 particles) was used for calculations.

$$Yield = \frac{r_{st.st} S_{total}}{g_{cat}} Ave_s \int_t PDF(s.t) dt \tag{11}$$

where S_{total} is the surface of all the particles (0.1m^2).

2.4. Mass transfer equations

Both diffusion and convection mass transfer were taken into account.

$$\nabla \cdot J_i + u \cdot \nabla c_i = R_i \tag{12}$$

$$J_i = -D_i \nabla c_i \tag{13}$$

Where J is Diffusive molar mass flux, u is the velocity; D is the diffusion coefficient; c is concentration, and R represents reaction. Due to the extremely low rate of the reaction, the resistance of the reaction is much higher than the diffusive mass transfer, so the mass transfer coefficient does not impact the outcome of the model. The concentration of H_2O, CO_2 and N_2 at the inlet is 0.5 mol.m^{-3}, 5 mol.m^{-3}and 94.5 mol.m^{-3} respectively.

2.5. Optics equations

PDF(t) is a function of intensity, so optics modelling was required for this simulation and COMSOL's ray tracing module was used for this purpose. The information on the experimental setup is shown in Table 3 (Lo et al., 2007).

A quarter of each lamp was defined as the light source, and the number of rays was set for those areas. All rays are assumed to be perpendicular to the surface of the lamp. Then, two accumulators were placed on the particle's surface to calculate the total number of rays and intensity on each mesh's element to acquire the average intensity of each mesh's element. Further explanation about the relation between the number of rays and mesh quality has been brought up in the mesh section of this article.

The direction of the refracted ray is computed using Snell's law based on the refractive index on either side.

$$n_1 \sin\theta_1 = n_2 \sin\theta_2 \tag{14}$$

where n is the refractive index, and θ_1 and θ_2 are the incidence and refraction angles, respectively.

Aside from refracted rays, the reflected rays must be calculated to obtain an accurate light distribution through the reactor. The values of intensity of the refracted and reflected rays are calculated by the Fresnel equation.

$$r_s = \frac{n_1 \cos\theta_i - n_2 \cos\theta_t}{n_1 \cos\theta_i + n_2 \cos\theta_t} \tag{15}$$

$$t_s = \frac{2 n_1 \cos\theta_i}{n_1 \cos\theta_i + n_2 \cos\theta_t} \tag{16}$$

$$r_p = \frac{n_2 \cos\theta_i - n_1 \cos\theta_t}{n_2 \cos\theta_i + n_1 \cos\theta_t} \tag{17}$$

$$t_p = \frac{2 n_1 \cos\theta_i}{n_2 \cos\theta_i + n_1 \cos\theta_t} \tag{18}$$

The equations consider a plane wave incident on a plane interface at an angle of incidence θ_i, a wave reflected at angle $\theta_r = \theta_i$, and a wave transmitted at angle θ_t. r_s and r_p are the reflection coefficient of s-polarized and p-polarized light. t_s and t_p are transmission coefficients of s-polarized and p-polarized light used to calculate reflectance and transmittance.

$$R = |r|^2 \tag{19}$$

$$T = \frac{n_2 \cos\theta_t}{n_1 \cos\theta_i} |t|^2 \tag{20}$$

where R is the reflectance which determines the fraction of irradiance reflected from the interface and T is the transmittance which is the fraction of irradiance refracted into the second medium. Threshold intensity is defined to stop the process of producing reflected rays and avoid excess calculation. It is clear that the threshold intensity must be considerably lower than the initial intensity to generate reflected rays as much as possible. Therefore, in this case, the threshold intensity equals 1 mW/m^2. All the pellets are considered as a material discontinuity and the optics equation applied on them. Due to relatively low pressure (1.1 atm) of the reactor, the unmeshed exterior domain between the particles assumed to be absolute vacuum which makes light distribution independent of the hydrodynamics. Therefore, the hydrodynamics only affect the steady state part of the reaction rate. It is worth mentioning that in the reactors with liquid phase such as slurry reactors, the absorption and scattering effects of the liquid which is itself a function of hydrodynamics of the reactor must be taken into account. Therefore both flow and radiation fields should be solved simultaneously (Boyjoo et al., 2013).

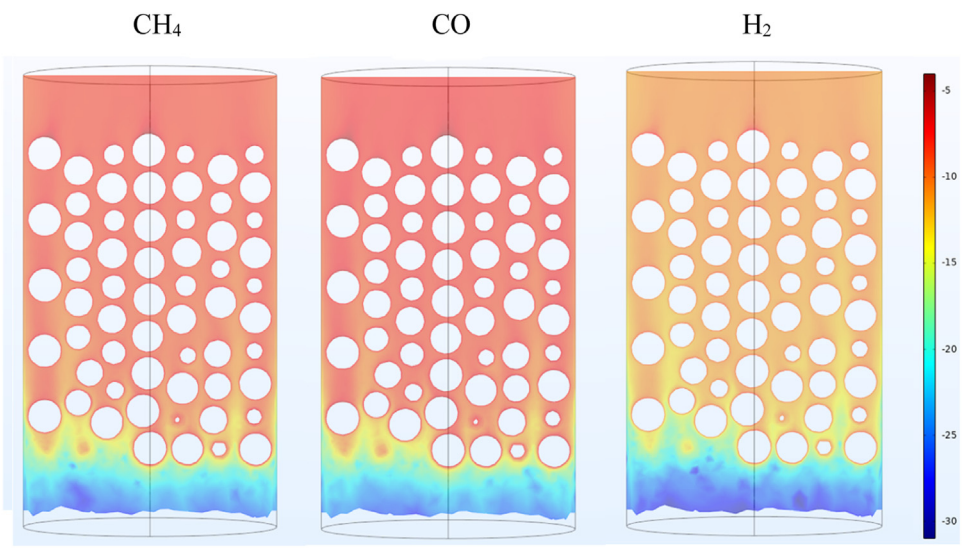

Fig. 4. Logarithmic concentration.

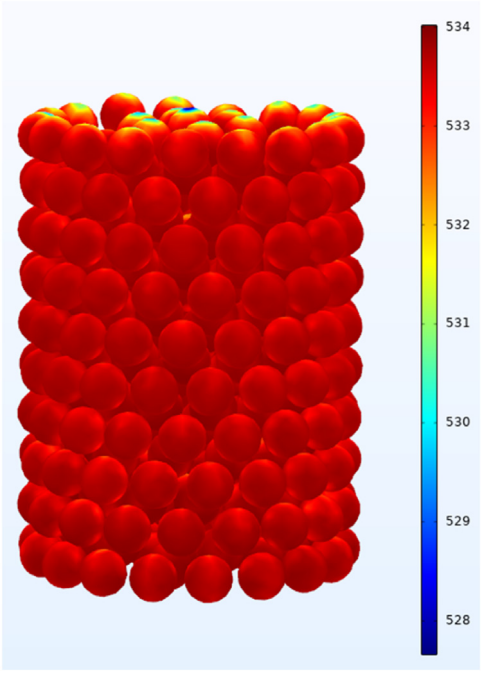

Fig. 5. The imaginary steady-state surface reaction of methane μmol.m^{-2}.h^{-1}.

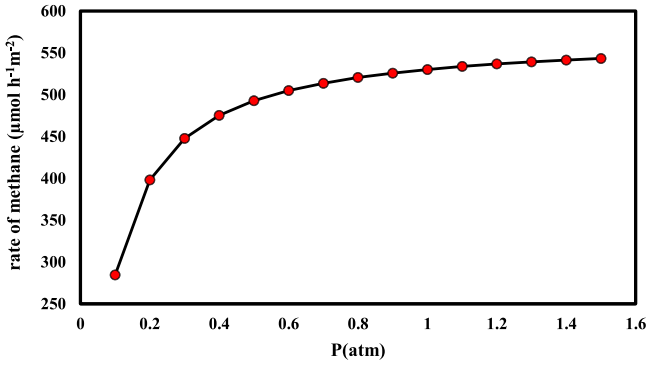

Fig. 6. Steady state rate of reaction over pressure.

3. Computational Fluid Dynamics

Due to the impact of light intensity on the reaction rate, optics modelling is needed for this case. To acquire a precise result of the light profile through the reactor, 3D modelling is inevitable as all the rays must be traced one by one in the rector. 3D modelling of several coupled equations (hydrodynamics, mass transfer, reaction and optics) in a packed bed reactor requires significant calculations, making the CFD technique a suitable solution for this case. The first step is generating the reactor's geometry in the blender, importing mesh to COMSOL Multiphysics, and applying all the equations.

3.1. The geometry of the reactor

The model is a circulated photocatalytic cylindric reactor filled with sphere particles. The packed bed photo-reactor was made from a quartz tube with length of 480 mm and the diameter of 22.5 mm. Pellets were made by pyrex to minimize the impacts of light absorption. All the pellets have the same diameter (3 mm) and they are pre-immobilized with anatase titanium dioxide powder (TiO_2) (Degussa, P-25) and the thickness of TiO_2 layer is around 145 μm (Lo et al., 2007). Also, for comparison, a model was developed for the Raschig pellet. Fig. 1 shows the reactor's geometry. The inner diameter of Raschig pellets is 2 mm, the outer diameter is 3 mm, and their height is 3 mm.

3.2. Generating the packed bed reactor

A random packed bed of spheres was generated by a novel method in the blender. All particles were randomly generated by a plane and then fell into the cylindric body of the reactor. Rigid body physics was applied to particles and the reactor body. Table 4 shows the parameters of the applied rigid body physics for the particles and the reactor's body.

After applying rigid body physics, the blender ran until it reached the 25000th frame. It is necessary to set sufficient time to ensure every particle gets stable. It is necessary to set a tiny margin between the particles in order to prevent contacting particles which leads to intersection error while building meshes in the next stages of simulation. Then all the particles were imported into COMSOL Multiphysics. Finally, a cylinder was generated in COMSOL, and a different method was used to acquire a PBR with just one domine. This process is to avoid any possible mesh generation or convergence error in the future. A randomly packed bed of Raschig rings was also generated to compare the optics.

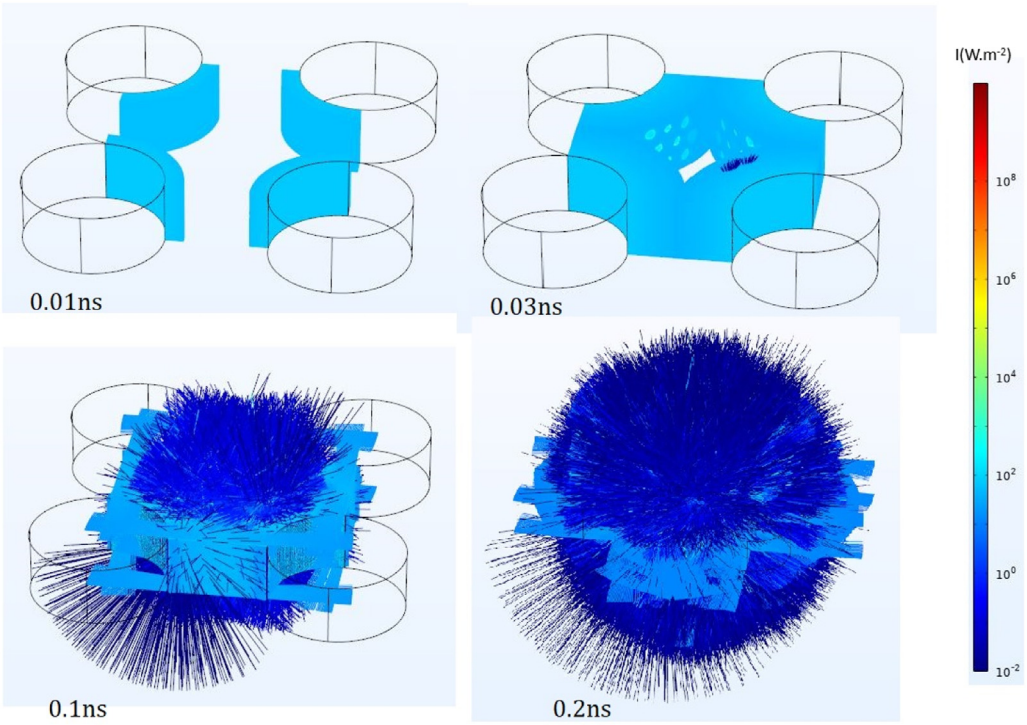

Fig. 7. Ray trajectories in 0.01 ns, 0.03 ns, 0.1 ns and 0.2 ns.

4. Result and discussion

In the first part, we will discuss the result of the imaginary steady-state model, including flow and concentration distribution through the reactor. In the second part, we will discuss the consequence of the unsteady state model, including light profile and blockage of the catalyst's surface over time. The results of both the steady-state model and light intensity through the reactor are necessary to obtain a time-dependant model.

4.1. Imaginary steady-state part

In this part, all the effects of the catalyst's surface blockage were ignored, and the case was assumed to be a steady state, i.e., only the steady state part of the reaction rate was used. The Reynolds number for an inlet velocity of 2 cm/s is 8.74, which is in the laminar regime, so the laminar equation is set for this model. Fig. 2a is a slice of the velocity profile in the reactor. The velocity sees noticeable changes through the reactor, which peaks at 14 cm/s. However, despite the considerable differences in velocity, the pressure remained almost steady because of the low inlet velocity (Fig. 2b).

The concentration profile of all products indicates a relatively low rate of reaction. However, changes in the concentration can only be seen in a thin layer outside of the particles (Fig. 3), so a logarithmic concentration profile was used to clearly show concentration changes through the reactor (Fig. 4).

Using a logarithmic concentration profile gives us a great sight into changes in concentration through the reactor (Fig. 4). In terms of concentration, CO has the highest, and then CH_4 and H_2 have the least concentration. To have a numeric comparison between products, the average rates of surface reactions were calculated for CH_4, CO and H_2, and the results were 533.70 $\mu mol.m^{-2}.h^{-1}$, 876.16 $\mu mol.m^{-2}.h^{-1}$ and 48.79 $\mu mol.m^{-2}.h^{-1}$, respectively. The steady-state part of the reaction is just a function of partial pressures, and because of minimal changes in partial pressure, it remained almost steady throughout the reactor. The 3D plot of methane's surface reaction (Fig. 5) proves this.

Fig. 6 is the diagram of the rate of methane production over the reactor's pressure, which indicates that the rate increases with the pressure; however, for pressures over atmospheric pressure, the rate has a slight functionality of pressure.

4.2. Time-dependant part and optics modelling

In the raytracing technique, all the rays are traced individually over time, so it is conceptually a time-dependant method so the critical question that is needed to be answered is how much time is enough to acquire a natural model of light distribution. All the rays must have enough time to completely pass through the reactor, which means there must be sufficient time for all the reflection. This crucial time is a function of the reactor's geometry. Fig. 7 shows the ray trajectories.

At 0.01 ns, the rays have not reached the particles. At 0.03 ns, the rays have just hit the particles. At 0.1 ns, the light reflections are still happening, and after 0.2 ns, the process of reflections has ended, and all the rays have passed through the reactor, which means all the rays' vectors are in the opposite direction of the reactor. As a result, after 2 ns, the profile of light intensity on the catalyst's surface will not experience any changes. To calculate adequate time for raytracing, the average intensity on the particles' surface over time is shown in Fig. 8.

At 0.03 ns all the rays reached the particles and after that the intensity on the particles begin to increase. After 0.15 ns the diagram is steady and see no changes over time which means all the rays have passed through the reactor so 0.15 ns is adequate for this modelling. The results of intensity at 0.2 ns have been used for the reaction rate calculation.

With the aid of optics modelling, changes in each product over time were calculated, showing great insight into how products react to the catalyst's surface blocking. Also, the effect of geometry and light source placement were considered to trace light intensity on the surface of particles. Probability density functions were calculated for all the products shown in Fig. 9 to evaluate their sensitivity to undesired products blocking the surface. PDF(t) for each point of the reactor is calculated by using the amount of light intensity on the surface of the particles. Fig. 9 shows

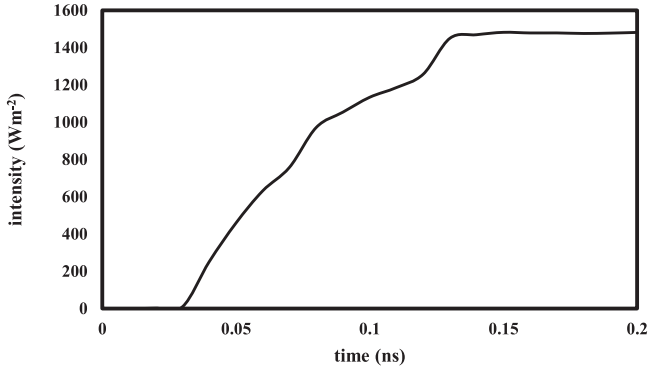

Fig. 8. Average intensity on the particles' surface over time.

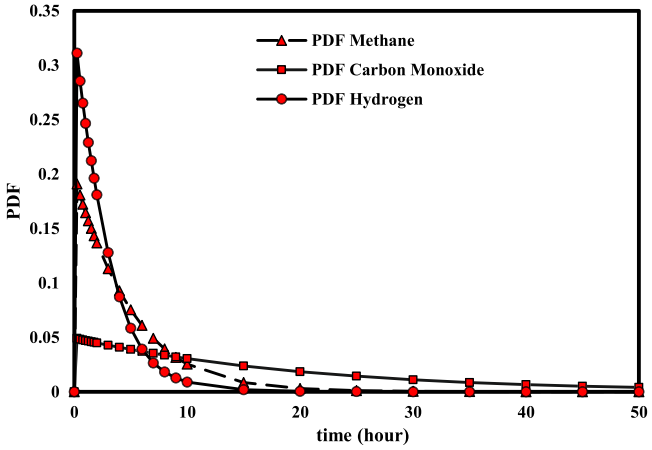

Fig. 9. Probability density function of CH_4, CO and H_2 over 50 h.

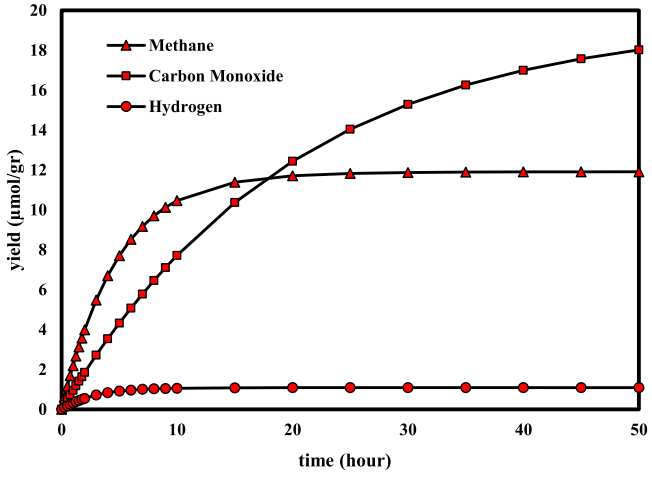

Fig. 10. Yield of CH_4, CO and H_2 over 50 h.

the surface average of PDF(t). At the start, hydrogen has the highest amount of PDF; however, its sensitivity to surface blockage is significantly higher than other species and its PDF after 6 h places lower than other species. After 15 h, the hydrogen generation process almost stops. In terms of sensitivity, CO is the one with the lowest. It outweighs CH_4 at the tenth hour, and its production continues even after 50 h.

Fig. 10 illustrates the yield of products over time. It is calculated using the amounts of PDF(t) and the imaginary steady-state rate of the reaction. Despite PDF, the steady state part of the reaction rate has a role in yield, and due to this fact, hydrogen generation is far less than other products. At first, the amount of methane's yield is the highest, and after 17 h, it is outweighed by CO. It is evident that the scopes of all diagrams gradually decrease over time because of the surface blockage.

Fig. 11 also shows how reaction rate can be affected by light intensity distribution. At 0.25 h, changes in reaction rates are much more evident than in the following moments since intensity is considerably variable through the particles, and so at first moments, there is a competition between the catalyst's sites and the ones with higher intensity have higher potential for reaction; but this also means that these sites stem from by-products blocking surface more; which leads to uniformity of reaction rates over time.

The shape of particles impacts light distribution and, along with that, the reaction rates. Therefore, a model with Raschig rings (r_1=2 mm r_2=3 mm h=3 mm) was developed and run to compare with previous results of spherical particles. Fig. 12 shows higher intensity and better uniformity in light distribution for spherical particles.

As shown in Fig. 13, the amount of PDF for the reactor with Raschig rings is higher at the beginning moments. Then after 1 h, it drops behind the spherical particles of the reactor, which is expected because the surfaces below the diagrams are equal to one.

Both number and placement of light resources affect the light distribution through the reactor. Increasing the number of lamps increases light intensity uniformity through the reactor. To investigate the impact of light recourses a case with 2 lamps opposite to each other has been modelled and the result of PDF is compared with the original model with 4 lamps (Fig. 14).

In terms of the case with 2 lamps, at the initial moments the regions closer to lamps exposed to higher light intensity and as a result the rate of catalyst's site blockage is higher. After a while, the released light will be blocked which results in poor light distribution in the reactor. By increasing the number of light sources, the catalyst's active sites deactivate over time more uniformly which results in better light distribution. By comparing the results of these 2 cases, it is evident that after about one hour of irradiation, the PDF of the case with 2 lamps falls behind the PDF of the case with 4 lamps due to its inferior light distribution.

Table 5 summarizes a number of CFD computational models presented in the open literature. Eulerian and Lagrangian are the main approaches for modelling the hydrodynamics of bubble slurry. Radiative transfer equation (RTE) is mainly used for optics modelling so far. The comparison between RTE and raytracing method in terms of accuracy and computational cost is worth further investigation in the future.

5. Mesh study

The properties of two types of mesh for steady state and optics modelling are investigated here:

5.1. Steady-state modelling of transport of phenomenon

A coarse element size was used for this model. To evaluate its accuracy, it is compared with coarser elements size. The similar results of the imaginary steady-state rate of reaction for all three products indicate the size of that coarse element is sufficient for this model. The meshes, their statics and their results are shown in Fig. 15 and Table 6.

5.2. Optics modelling

Despite the transport of phenomenon simulations, in optics modelling, the calculation accuracy does not just depend on mesh; the number of rays plays a vital part in this case. Smaller mesh elements size leads to more accurate light distribution, but the downside is a higher number of rays is required, which costs more time and calculation resources. In other words, each element size requires a minimum number of rays to satisfy it. Therefore, the fine and finer mesh was used in this study. The meshes and their statics are shown in Fig. 16 and Table 7.

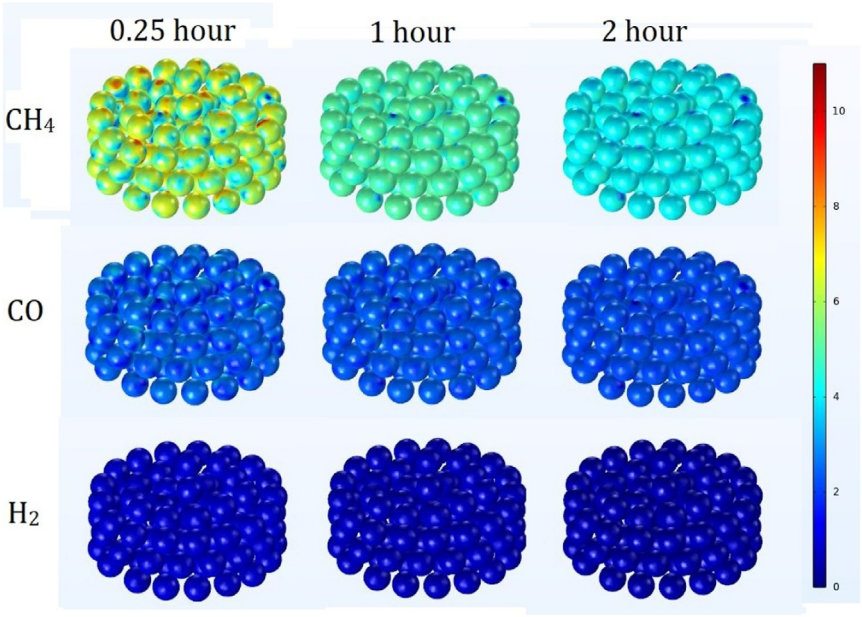

Fig. 11. The surface reaction rate (μmol.m^{-2}.h^{-1}) of CH_4 (first row), CO (second row) and H_2 (third row) after 0.25 h (first column), 1 h (second column) and 2 h (third column).

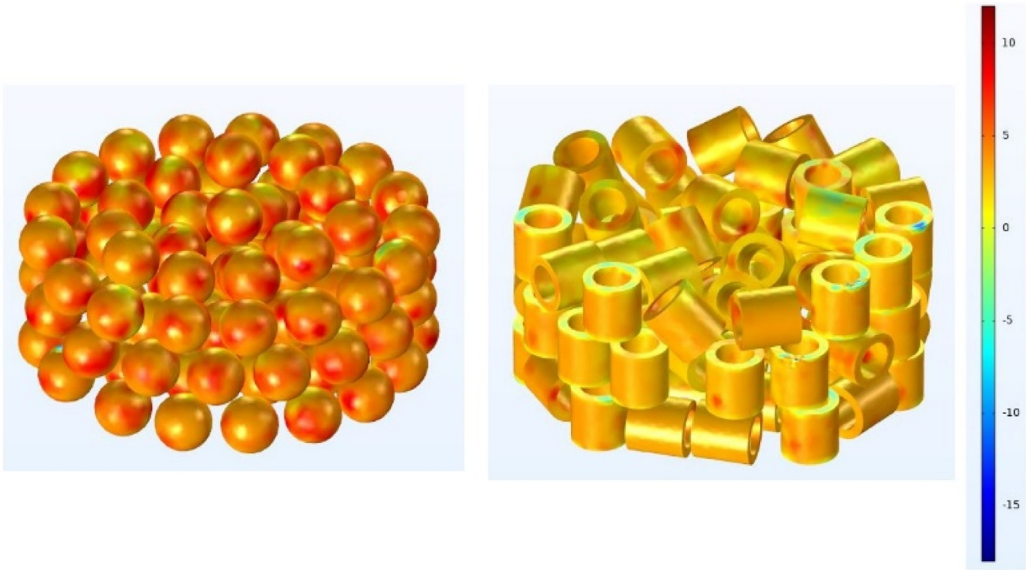

Fig. 12. Logarithmic intensity (W.m^{-2}) profile of spherical and cylindrical particles.

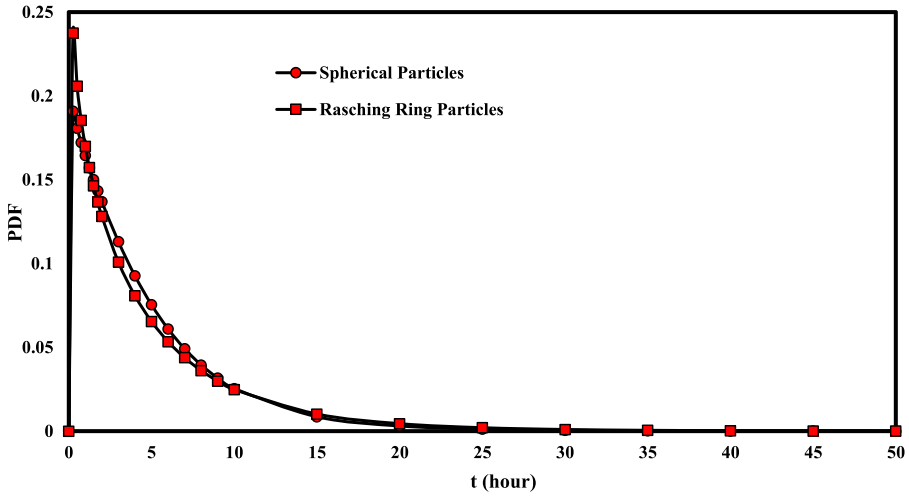

Fig. 13. The probability density function of methane for spherical and Raschig particles.

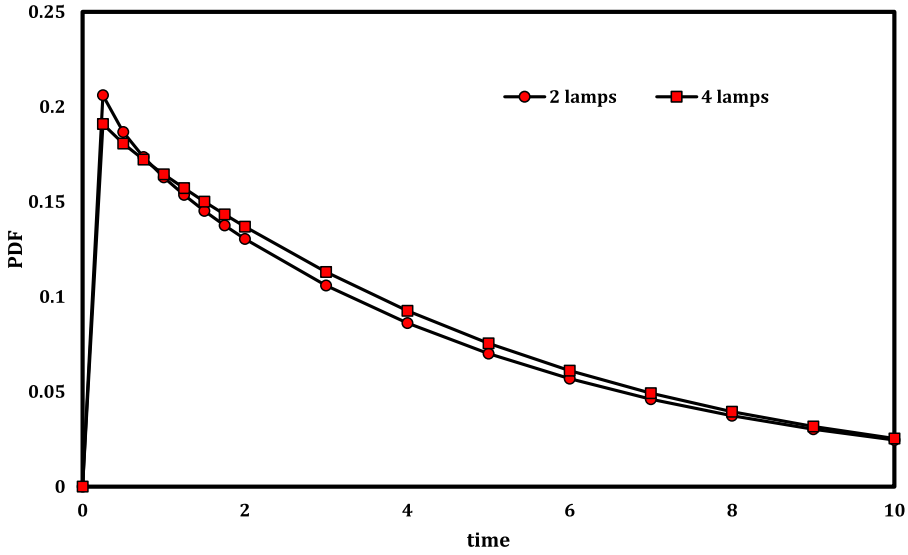

Fig. 14. The probability density function of methane for 2 lamps and 4 lamps.

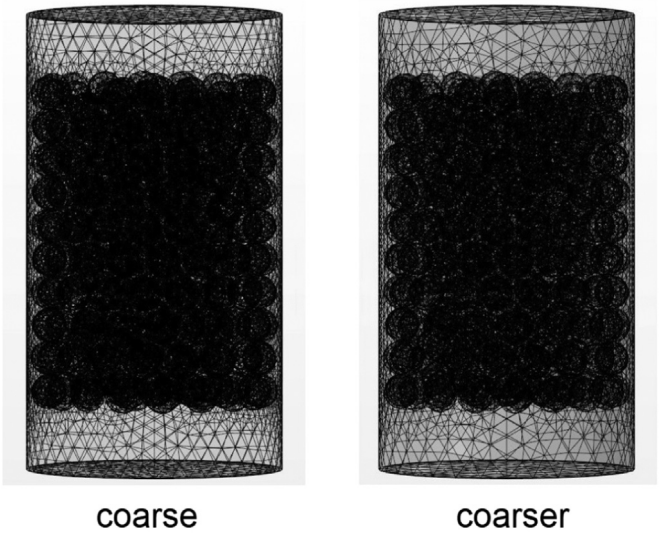

Fig. 15. Two types of mesh for steady-state modelling.

Table 6
Mesh statics for the steady-state part of the study.

Mesh properties	Coarse	Coarser
tetrahedra	432,004	194,300
prisms	164,156	92,944
triangles	82,732	46,848
quads	192	128
Edge elements	281	203
Vertex elements	8	8
Number of elements	596,160	287,244
r(st.st) CH_4	533.70	533.78
r(st.st) CO	876.16	876.41
r(st.st) H_2	49.80	48.83

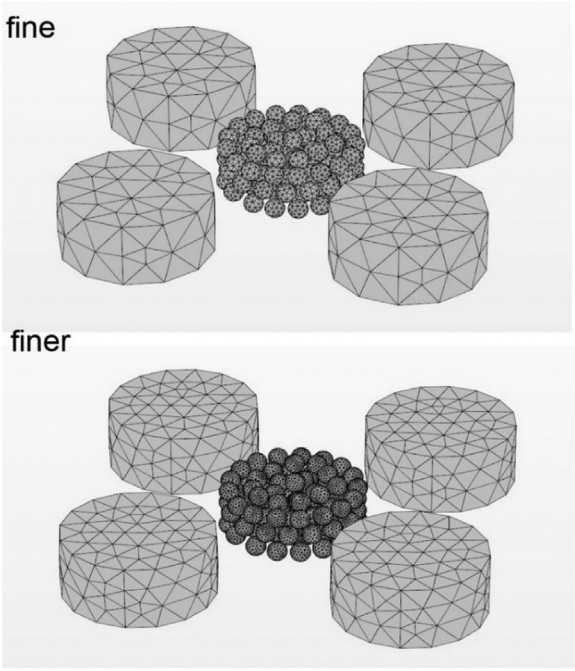

Fig. 16. Two types of mesh for the optics modelling part of the study.

Table 7
Mesh statistics for optics modelling part of the study.

Mesh properties	Fine	finer
tetrahedra	20,923	104,878
triangles	10,680	31,506
Edge elements	128	176
Vertex elements	32	32
Number of elements	20,923	104,878

It should be noted that lamps' meshes are not crucial in this case because the initial position of the released rays was defined as density based, not mesh-based.

There are two ways to determine the minimum number of rays. One way is increasing the number of rays until reaching a constant probability density function; if the number of rays is not sufficient, increasing it increases PDF. The more practical way is calculating the surface below the PDF over a long time, like 10,000 h, which is used for this case. If the integral of PDF is close to one, the number of rays is adequate. Both methods were used in these 4 cases; the results are evident in Fig. 17 and Table 8. The four cases considered, are Case 1: mesh fine 200,000 rays (used in this project), Case 2: mesh fine 160,000 rays, Case 3: mesh fine

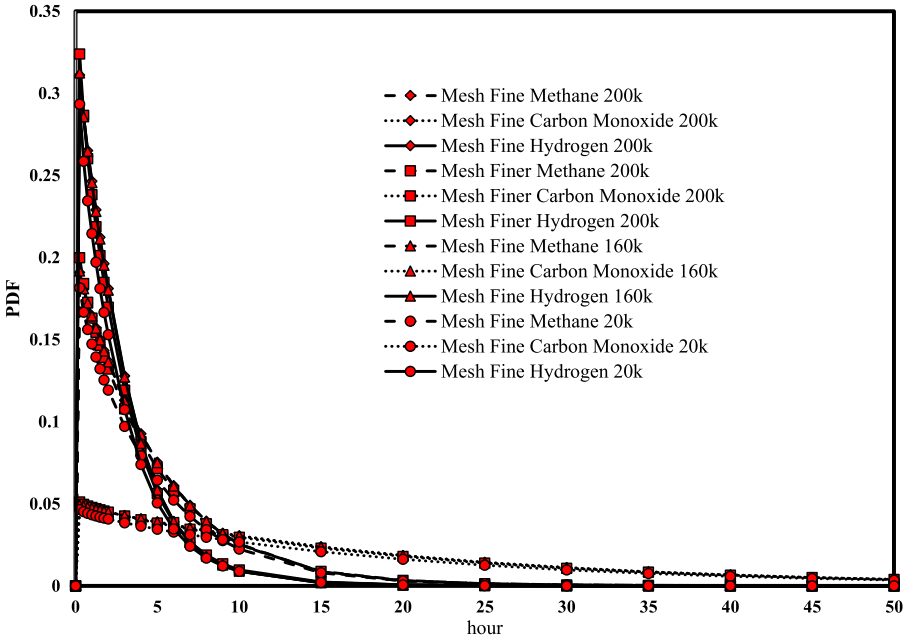

Fig. 17. The probability density function of products for all cases of mesh study.

Table 8
Mesh study cases.

Product	Mesh	Number of rays	Integral of PDF
CH_4	fine	200k	0.99647
		160k	0.99504
		20k	0.88523
	finer	200k	0.97937
CO	fine	200k	0.99649
		160k	0.99504
		20k	0.88525
	finer	200k	0.97939
H_2	fine	200k	0.99642
		160k	0.99503
		20k	0.88518
	finer	200k	0.97933

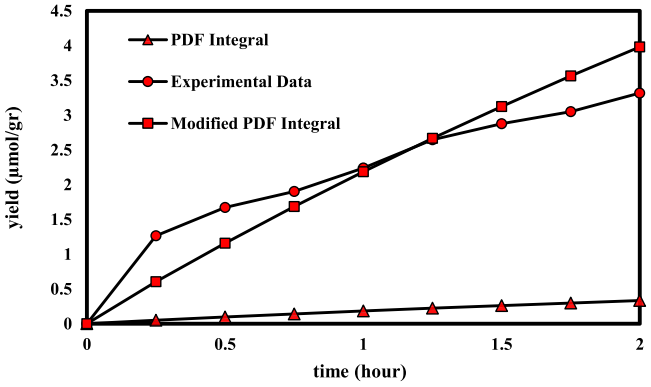

Fig. 18. Validation of yield with experimental data.

20,000 rays and Case 4: mesh finer 200,000 rays. All the cases almost fit together (Fig. 17).

The integral of PDF for both 200k rays (fine mesh) and 160k rays (fine mesh) is higher than 0.99, which shows the number of rays is adequate for both of them. The integral of PDF for 20k rays is 0.88 for all products, meaning the number of rays is insufficient. The integral of PDF for finer mesh with 200k is 0.97, which illustrates that 200k rays are enough, even for finer mesh, so 200k rays are adequate for fine mesh.

6. Validation with the experimental results

At first, the integral of PDF over time was calculated for methane and then compared with the experimental yield result. The extracted experimental data examined the yield of the reactor over time (Lo et al., 2007). It is evident that both diagrams follow similar trends, and both of them decrease over time as a result of the catalyst's surface blockage (Fig. 18).

Based on Eq. (10), the ratio of yields to the integral of PDF is constant so that the equation can be rewritten like this:

$$\frac{\sum Yield}{\sum Ave_s\left(\int_t PDFdt\right)} = \frac{r_{st.st}S_{total}}{g_{cat}} = 11.10 \tag{21}$$

The overall catalyst's surface and the catalyst's mass are equal to $0.1m^2$ and 0.25 g, respectively, so the $r_{st.st}$ of methane is expected to be 27.75; however, because of the lack of information about the amount of surface catalyst coverage in the experimental setup and its effect on reaction rate we need to define a correction coefficient(C) for $r_{st.st}$ by the aid of its calculated result (533.7) and then expand it to the other products. As a result, Eq. (10) turns into Eq. (21).

$$C = \frac{r(e)_{st.st}}{r(c)_{st.st}} = 0.052 \tag{22}$$

$$Yield = C\,\frac{r_{st.st}S_{total}}{g_{cat}}Ave_s\int_t PDFdt \tag{23}$$

C is the correction coefficient, and r(e) and r(c) are the experimental and calculated results of the steady-state part of the reaction rate. The standard error of the regression (SE) was used to show differences with the unit of µmol. $gcat^{-1}$ between the experimental yield data and the model used.

$$SE = \sqrt{\frac{\sum (Y_m - Y_e)^2}{N-2}} \tag{24}$$

where SE is the standard error of regression of the yield of the model (µmol. $gcat^{-1}$); Y_m is a vector of the experimental yield data points (µmol. $gcat^{-1}$); Y_e is a vector of the predicted yield data points using the probability LH based kinetic model, and N is the number of experimental yield data points. in the first two hours, the yield experiences

the most changes over time with SE error of 0.22 (μmol. $gcat^{-1}$), and after two hours the amount of yield gradually tends to a constant value as the reaction rate tends to zero.

7. Conclusion

Photo-reduction of CO_2 is an innovative approach to cope with the increasingly harmful consequences of the greenhouse effect. However, optimising this process has been challenging for researchers due to its complex reaction, which is tightly engaged with light distribution and various operational parameters. This study investigates the influence of operating parameters, reactor geometry, and the catalyst's surface blockage on products' yields. Generating a three-dimensional packed bed reactor's geometry was vital in optics modelling since a large number of rays must be traced through the reactor's space. With the blender's rigid body physics, all the pellets were dropped onto the reactor to simulate real-world situations. As a result, a precise 3D random-packed bed has been generated with both sphere and Raschig ring pellets. For the first time, a method has been introduced to trace rays through a photocatalytic packed bed reactor which is known to be geometrically one of the most complex reactors. This step is the most time-consuming part of the modelling since the number of rays must satisfy the reactor's mesh. Finding a relation between mesh quality and rays' number was a series challenge because several case studies had to be defined to find the sufficient number of rays for each mesh quality. This new technique aids us in calculating the profile of light intensity on the particles' surface and seeing the catalyst's site blockage over time. All this process needs a considerable amount of calculation which, thanks to recent development in technology and processing unit, has become feasible for such cases. Furthermore, this technique could be expanded to other models engaged with optics modelling and aids researchers in getting through the challenges involved in such areas; For example, in packed bed reactors with increasing the cross-sectional area and consequent increment of the number of particles, the number of secondary rays will exponentially increase which directly affects the calculation cost. The best way to decrease time and cost of calculation is to use GPU instead of CPU, because the calculation of raytracing is parallel, however common CFD software do not utilize GPU for raytracing yet (Nordmark, 2022). Modelling of photo-reduction of CO_2 in a packed bed reactor gave us valuable information about changes in rates of reactions over time and products' sensitivity to time. The sensitivity of H_2 and CO are the highest and lowest, respectively, which fully supports experimental data; however, further experimental analysis is needed for the impact of the surface catalyst's coverage and light intensity to acquire a precise, comprehensive model for this particular reaction.

Declaration of Competing Interest

The authors declare that they have no known competing financial interests or personal relationships that could have appeared to influence the work reported in this paper.

Acknowledgement

No funding was available for this study.

References

IPCC. Climate change 2014: synthesis report. Contribution. 2014.
IPPC, Roberts D., Pidcock R., Chen Y., Connors S., Tignor M. Science Editor 2018.
Fasihi, M., Efimova, O., Breyer, C., 2019. Techno-economic assessment of CO_2 direct air capture plants. J. Clean. Prod. 224, 957–980. doi:10.1016/j.jclepro.2019.03.086.
Vitillo, J.G., Smit, B., Gagliardi, L., 2017. Introduction: carbon capture and separation. Chem. Rev. 117, 9521–9523. doi:10.1021/acs.chemrev.7b00403.
Borhani, T.N., Wang, M., 2019. Role of solvents in CO_2 capture processes: the review of selection and design methods. Renew. Sustain. Energy Rev. 114, 109299. doi:10.1016/j.rser.2019.109299.
Nematollahi R., Ghotbi C., Khorasheh F., Larimi A., Moradi M. Sol-gel derived Bismuth modified TiO2, a highly visible light response nano-photocatalyst for CO 2 photoreduction 2019:20–2.
Nematollahi, R., Ghotbi, C., Khorasheh, F., Larimi, A., 2020. Ni-Bi co-doped TiO_2 as highly visible light response nano-photocatalyst for CO_2 photo-reduction in a batch photoreactor. J. CO2 Util. 41. doi:10.1016/j.jcou.2020.101289.
Moradi M., Khorasheh F., Larimi A., Nematollahi R. Photo-assisted deposition of Pt nanoparticles onto TiO2 as highly active nano- photocatalyst for CO2 photoreduction 2019:20–2.
Moradi, M., Khorasheh, F., Larimi, A., 2020. Pt nanoparticles decorated Bi-doped TiO_2 as an efficient photocatalyst for CO_2 photo-reduction into CH_4. Sol. Energy 211, 100–110. doi:10.1016/j.solener.2020.09.054.
Larimi, A., Khorasheh, F., 2020. Carbonaceous supports decorated with Pt–TiO_2 nanoparticles using electrostatic self-assembly method as a highly visible-light active photocatalyst for CO_2 photoreduction. Renew. Energy 145, 1862–1869. doi:10.1016/j.renene.2019.07.105.
Yao, B., Xiao, T., Makgae, O.A., Jie, X., Gonzalez-Cortes, S., Guan, S., et al., 2020. Transforming carbon dioxide into jet fuel using an organic combustion-synthesized Fe-Mn-K catalyst. Nat. Commun. 11. doi:10.1038/s41467-020-20214-z.
Garba, M.D., Usman, M., Khan, S., Shehzad, F., Galadima, A., Ehsan, M.F., et al., 2021. CO_2 towards fuels: a review of catalytic conversion of carbon dioxide to hydrocarbons. J. Environ. Chem. Eng. 9, 104756. doi:10.1016/j.jece.2020.104756.
Whang, H.S., Lim, J., Choi, M.S., Lee, J., Lee, H., 2019. Heterogeneous catalysts for catalytic CO_2 conversion into value-added chemicals. BMC Chem. Eng. 1, 1–19. doi:10.1186/s42480-019-0007-7.
Pakhare, D., Spivey, J., 2014. A review of dry (CO_2) reforming of methane over noble metal catalysts. Chem. Soc. Rev. 43, 7813–7837. doi:10.1039/c3cs60395d.
Chen, X., Su, X., Duan, H., Liang, B., Huang, Y., Zhang, T., 2017. Catalytic performance of the Pt/TiO_2 catalysts in reverse water gas shift reaction: controlled product selectivity and a mechanism study. Catal. Today 281, 312–318. doi:10.1016/j.cattod.2016.03.020.
Zhu, D.D., Liu, J.L., Qiao, S.Z., 2016. Recent advances in inorganic heterogeneous electrocatalysts for reduction of carbon dioxide. Adv. Mater. 28, 3423–3452. doi:10.1002/adma.201504766.
Creutzig, F., Agoston, P., Goldschmidt, J.C., Luderer, G., Nemet, G., Pietzcker, R.C., 2017. The underestimated potential of solar energy to mitigate climate change. Nat. Energy 2. doi:10.1038/nenergy.2017.140.
Alsayegh, S.O., Varjian, R., Alsalik, Y., Katsiev, K., Isimjan, T.T., Idriss, H., 2020. Methanol production using ultrahigh concentrated solar cells: hybrid electrolysis and CO_2 capture. ACS Energy Lett. 5, 540–544. doi:10.1021/acsenergylett.9b02455.
Olivo, A., Trevisan, V., Ghedini, E., Pinna, F., Bianchi, C.L., Naldoni, A., et al., 2015. CO_2 photoreduction with water: catalyst and process investigation. J. CO2 Util. 12, 86–94. doi:10.1016/j.jcou.2015.06.001.
Zhang, Z., Wang, Y., Cui, G., Liu, H., Abanades, S., Lu, H., 2021. Improvement of CO_2 photoreduction efficiency by process intensification. Catalysts 11. doi:10.3390/catal11080912.
Kovačič, Ž., Likozar, B., Huš, M., 2020. Photocatalytic CO_2 reduction: a review of ab initio mechanism, kinetics, and multiscale modeling simulations. ACS Catal. 14984–15007. doi:10.1021/acscatal.0c02557.
Gandhi, R., Moses, A., Baral, S.S., 2022. Fundamental study of the photocatalytic reduction of CO_2: a short review of thermodynamics, kinetics and mechanisms. Chem. Process Eng. 43, 223–228. doi:10.24425/cpe.2022.140825, Inz Chem i Proces.
Ji, Y., Luo, Y., 2016. New mechanism for photocatalytic reduction of CO_2 on the anatase TiO_2(101) surface: the essential role of oxygen vacancy. J. Am. Chem. Soc. 138, 15896–15902. doi:10.1021/jacs.6b05695.
Li, K., Peng, B., Peng, T., 2016. Recent advances in heterogeneous photocatalytic CO_2 conversion to solar fuels. ACS Catal. 6, 7485–7527. doi:10.1021/acscatal.6b02089.
Ola, O., Maroto-Valer, M.M., 2015. Review of material design and reactor engineering on TiO_2 photocatalysis for CO_2 reduction. J. Photochem. Photobiol. C Photochem. Rev. 24, 16–42. doi:10.1016/j.jphotochemrev.2015.06.001.
Asadi, A., Larimi, A., Jiang, Z., Naderifar, A., 2022. Modeling and simulation of photocatalytic CO_2 reduction into methanol in a bubble slurry photoreactor. Chem. Eng. Sci. 263, 118078. doi:10.1016/J.CES.2022.118078.
Baker M.J. CFD simulation of flow through packed beds using the finite volume technique. Univ Exet 2011:208.
Ali, S., Flores, M.C., Razzaq, A., Sorcar, S., Hiragond, C.B., Kim, H.R., et al., 2019. Gas phase photocatalytic CO_2 reduction, "a brief overview for benchmarking. Catalysts 9, 1–26. doi:10.3390/catal9090727.
Thompson, W.A., Sanchez Fernandez, E., Maroto-Valer, M.M., 2020a. Review and analysis of CO_2 photoreduction kinetics. ACS Sustain. Chem. Eng. 8, 4677–4692. doi:10.1021/acssuschemeng.9b06170.
Delavari, S., Amin, N.A.S., 2016. Photocatalytic conversion of CO_2 and CH4 over immobilized titania nanoparticles coated on mesh: optimization and kinetic study. Appl. Energy 162, 1171–1185. doi:10.1016/j.apenergy.2015.03.125.
Khalilzadeh, A., Shariati, A., 2018. Photoreduction of CO_2 over heterogeneous modified TiO_2 nanoparticles under visible light irradiation: synthesis, process and kinetic study. Sol. Energy 164, 251–261. doi:10.1016/j.solener.2018.02.063.
Kwon, S., Liao, P., Stair, P.C., Snurr, R.Q., 2016. Alkaline-earth metal-oxide overlayers on TiO_2: application toward CO_2 photoreduction. Catal. Sci. Technol. 6, 7885–7895. doi:10.1039/c6cy01661h.
Shakeri, J., Farrokhpour, H., Hadadzadeh, H., Joshaghani, M., 2015. Photoreduction of CO_2 to CO by a mononuclear *Re*(i) complex and DFT evaluation of the photocatalytic mechanism. RSC Adv. 5, 41125–41134. doi:10.1039/c5ra02002f.
Shown, I., Samireddi, S., Chang, Y.C., Putikam, R., Chang, P.H., Sabbah, A., et al., 2018. Carbon-doped SnS_2 nanostructure as a high-efficiency solar fuel catalyst under visible light. Nat. Commun. 9. doi:10.1038/s41467-017-02547-4.

Tahir, M., Amin, N.A.S., 2015. Indium-doped TiO_2 nanoparticles for photocatalytic CO_2 reduction with H_2O vapors to CH4. Appl. Catal. B Environ. 162, 98–109. doi:10.1016/j.apcatb.2014.06.037.

Tan, L.L., Ong, W.J., Chai, S.P., Mohamed, A.R., 2017. Photocatalytic reduction of CO_2 with H_2O over graphene oxide-supported oxygen-rich TiO_2 hybrid photocatalyst under visible light irradiation: process and kinetic studies. Chem. Eng. J. 308, 248–255. doi:10.1016/j.cej.2016.09.050.

Aal E Ali, R.S., Zhou, Y., Gong, K., Jiang, X., 2022. Parallel photoreactor development with enhanced photon efficiency and reproducibility based on laws of optics. Green Synth. Catal. doi:10.1016/j.gresc.2022.10.007.

Martin, J., Dannenberg, A., Detrell, G., Ewald, R., Fasoulas, S., 2020. Maximizing nitrate absorption of agricultural waste water in a tubular microalgae reactor by adapting the illumination spectrum. Int. J. Agric. Biosyst. Eng. 14, 140–147.

Mazarji, M., Bidhendi, G.N., Mahmoodi, N.M., 2017. Mathematical modelling of an annular photocatalytic reactor for methylene blue degradation under UV light irradiation using rGO-ZnO hybrid. Prog. Color Color. Coat. 10, 173–180.

Szyman, J., 2021. Multiple steady states in the photocatalytic reactor for colored compounds degradation. Molecules 26. doi:10.3390/molecules26133804.

Mamouei, M., Budidha, K., Baishya, N., Qassem, M., Kyriacou, P.A., 2021. An empirical investigation of deviations from the Beer–Lambert law in optical estimation of lactate. Sci. Rep. 11, 1–9. doi:10.1038/s41598-021-92850-4.

Hossain, M.M., Raupp, G.B., 1998. Radiation field modeling in a photocatalytic monolith reactor. Chem. Eng. Sci. 53, 3771–3780. doi:10.1016/S0009-2509(98)00176-6.

Jiang, Y., Khadilkar, M.R., Al-Dahhan, M.H., Dudukovic, M.P., 2002. CFD of multiphase flow in packed-bed reactors: II. Results and applications. AIChE J. 48, 716–730. doi:10.1002/aic.690480407.

Thompson, W.A., Sanchez Fernandez, E., Maroto-Valer, M.M., 2020b. Probability Langmuir-Hinshelwood based CO_2 photoreduction kinetic models. Chem. Eng. J. 384, 123356. doi:10.1016/j.cej.2019.123356.

Fresno, F., Villar-García, I.J., Collado, L., Alfonso-González, E., Renones, P., Barawi, M., et al., 2018. Mechanistic view of the main current issues in photocatalytic CO_2 reduction. J. Phys. Chem. Lett. 9, 7192–7204. doi:10.1021/acs.jpclett.8b02336.

Lo, C.C., Hung, C.H., Yuan, C.S., Wu, J.F., 2007. Photoreduction of carbon dioxide with H_2 and H_2O over TiO_2 and ZrO_2 in a circulated photocatalytic reactor. Sol. Energy Mater. Sol. Cells 91, 1765–1774. doi:10.1016/j.solmat.2007.06.003.

Boyjoo, Y., Ang, M., Pareek, V., 2013. Some aspects of photocatalytic reactor modeling using computational fluid dynamics. Chem. Eng. Sci. 101, 764–784. doi:10.1016/j.ces.2013.06.035.

Lu, X., Tan, J.Z.Y., Maroto-Valer, M.M., 2022. Investigation of CO_2 photoreduction in an annular fluidized bed photoreactor by MP-PIC simulation. Ind. Eng. Chem. Res. 61, 3123–3136. doi:10.1021/acs.iecr.1c04035.

Lu, X., Luo, X., Tan, J.Z.Y., Maroto-Valer, M.M., 2021. Simulation of CO_2 photoreduction in a twin reactor by multiphysics models. Chem. Eng. Res. Des. 171, 125–138. doi:10.1016/j.cherd.2021.04.011.

Nordmark R. A ray tracing implementation performance comparison between the CPU and the GPU 2022.